

Dual-level Modality Debiasing Learning for Unsupervised Visible-Infrared Person Re-Identification^{*}

Jiaze Li^{a,1}, Yan Lu^{b,1}, Bin Liu^{a,*}, Guojun Yin^a, Mang Ye^c

^aUniversity of Science and Technology of China, Hefei, 230026, China

^bShanghai Artificial Intelligence Laboratory, Shanghai, 200233, China

^cthe School of Computer Science, Wuhan University, Wuhan, 430072, China

Abstract

Two-stage learning pipeline has achieved promising results in unsupervised visible-infrared person re-identification (USL-VI-ReID). It first performs single-modality learning and then operates cross-modality learning to tackle the modality discrepancy. Although promising, this pipeline inevitably introduces modality bias: modality-specific cues learned in the single-modality training naturally propagate into the following cross-modality learning, impairing identity discrimination and generalization. To address this issue, we propose a Dual-level Modality Debiasing Learning (DMDL) framework that implements debiasing at both the model and optimization levels. At the model level, we propose a Causality-inspired Adjustment Intervention (CAI) module that replaces likelihood-based modeling with causal modeling, preventing modality-induced spurious patterns from being introduced, leading to a low-biased model. At the optimization level, a Collaborative Bias-free Training (CBT) strategy is introduced to interrupt the propagation of modality bias across data, labels, and features by integrating modality-specific augmentation, label refinement, and feature alignment. Extensive experiments on benchmark datasets demonstrate that DMDL could enable modality-invariant feature learning and a more generalized model.

Keywords: Visible-infrared person re-identification, Unsupervised learning, Causal

^{*}This work is supported by the National Natural Science Foundation of China (Grant No. 62272430).

^{*}Corresponding author

Email addresses: jz_li@mail.ustc.edu.cn (Jiaze Li), luyan@pjlab.org.cn (Yan Lu), flowice@ustc.edu.cn (Bin Liu), gjyin@mail.ustc.edu.cn (Guojun Yin), yemang@whu.edu.cn (Mang Ye)

¹These authors contributed equally to this work.

1. Introduction

Visible-infrared person re-identification (VI-ReID) focuses on the identification and matching of individuals across distinct modalities, visible and infrared. Remarkable progress has been made in this field, as evidenced by the success of existing works [1, 2]. However, the collection of extensive cross-modality annotations is a costly and time-consuming process, which poses limitations on its broader application. As a solution, Unsupervised Visible-infrared Person Re-identification (USL-VI-ReID) [3, 4, 5] has emerged to facilitate VI-ReID without the reliance on human identity labels.

The main challenge in the USL-VI-ReID is the modality discrepancy, which limits the direct application of standard unsupervised learning of traditional unsupervised ReID. Therefore, the mainstream methods for USL-VI-ReID typically follow a two-stage learning pipeline [4, 5, 6, 7]: 1) In the first stage, the model is trained by operating unsupervised learning techniques [8] on each modality separately to have the single-modality discriminative ability. 2) In the second cross-modality unsupervised process, the model alternately establishes relationships across modalities and fits these relationships to achieve cross-modality discrimination capabilities. Although promising, it also suffers from a modality bias issue that restricts the overall results. The first single-modality learning process naturally captures modality-specific cues from visible/infrared data, resulting in a biased model. Initializing the second stage with this model inevitably introduces modality bias into the cross-modality learning, leading to biased cross-modality relationships, e.g., similar clothing color cues may result in incorrect matches across modalities, as illustrated in Fig. 1 (a). Since cross-modality relationships (i.e., pseudo labels) are the model-fitting target in the second stage, the biased knowledge (i.e., modality-specific cues) is gradually enhanced in the learned patterns, leading to modality-related features. In summary, modality bias originating from data propagates into labels and features throughout the learning pipeline, leading the model to rely on modality-specific cues for identification and thereby significantly limiting its generalization.

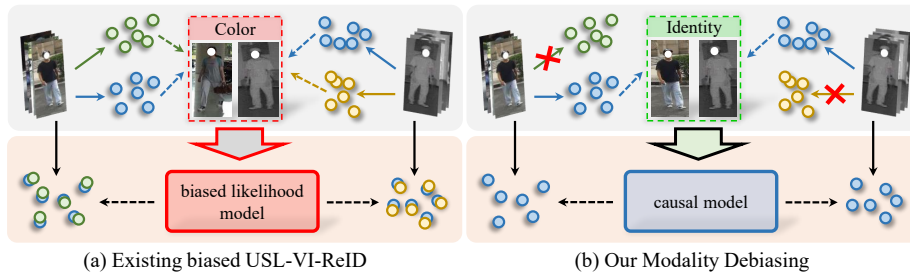


Figure 1: Existing USL-VI-ReID methods suffer from modality bias, leading to modality-related features. In contrast, our approach achieves modality-invariant feature learning through causal modeling and unbiased optimization. Green, yellow, and blue circles represent visible-specific, infrared-specific, and modality-shared information, respectively.

To address the aforementioned modality bias issue, we propose a Dual-level Modality Debiasing Learning (DMDL) framework. DMDL performs modality debiasing at both the model and optimization levels, where the former prevents the model from learning modality bias in incorrect cross-modality relationships, and the latter aims to disrupt the propagation of biased knowledge from data to labels and features directly. To this end, a Causality-inspired Adjustment Intervention (CAI) module and a Collaborative Bias-free Training (CBT) strategy are proposed. Specifically, CAI facilitates causal intervention under cross-modality unsupervised learning with backdoor adjustment, making the model only capture the causal patterns. Compared with the traditional likelihood method, the causal modeling in CAI is theoretically unaffected by modality bias, thereby achieving a low-biased model. To further prevent biased knowledge from deepening during optimization, we propose the CBT strategy, integrating data augmentation, label refinement, and feature alignment. CBT first introduces a pseudo-modality augmentation scheme to modify modality-specific cues in images. Based on the augmented images, a cross-modality label smoothing scheme and a feature alignment loss are proposed to refine the biased relationships and learn shared knowledge across pseudo-modalities, respectively. By jointly leveraging these components, CBT explicitly interrupts the propagation of modality bias across data, labels, and features. Ultimately, the overall DMDL keeps an effective modality debiasing implementation, achieving modality-invariant feature learning, as Fig. 1 (b) shows.

Our main contributions are summarized as follows:

- (1) We investigate the modality bias issue for existing USL-VI-ReID methods and propose a Dual-level Modality Debiasing Learning (DMDL) framework performed at both the model and optimization levels to learn modality-invariant feature representations.
- (2) We propose a Causality-inspired Adjustment Intervention (CAI) module at the model level to effectively model the causal patterns, constructing a low-biased model.
- (3) We propose a Collaborative Bias-free Training (CBT) strategy at the optimization level, combining label refinement and feature alignment with modality-specific data augmentation to prevent fitting biased knowledge.
- (4) Extensive experiments conducted on standard visible-infrared ReID benchmarks demonstrate the effectiveness and superiority of our method.

2. Related Work

2.1. Unsupervised Visible-Infrared Person ReID

Due to the advantage of not relying on any human annotations, USL-VI-ReID has attracted increasing attention. Most existing approaches adopted a two-stage pipeline to mitigate the significant modality discrepancy, and most of them aimed at exploring reliable cross-modality correspondences. For instance, PGM [4] and MBCCM [5] utilized graph matching to establish reliable relationships across modalities globally, while DOTLA [9] leveraged optimal transport for cross-modality matching. Other methods, such as MULT [10] and DLM [11], designed a more complex matching scheme by integrating cluster-level matching with instance-level structures to enhance the reliability of cross-modality association. Moreover, PCLHD [6] revisited prototype construction in contrastive learning to explore more reliable clustering. Despite their effectiveness, these methods are inherently constrained by the two-stage pipeline, which inevitably introduces modality bias and hinders the modality-invariant learning.

In addition, some methods [12, 13, 14] only perform a single stage of cross-modality learning. Specifically, GUR [12] proposed a bottom-up domain learning strategy that

performs intra-camera training, inter-camera training, and inter-modality training alternately. CHCR [13] designed a cross-modality hierarchical clustering baseline that first refines clusters within each modality before merging them cross-modally based on similarity. SDCL [14] proposed a shallow-deep collaborative learning framework that initializes with a pre-trained model of single-modality ReID. Although explicitly abandoning the two-stage pipeline, these methods still suffer from the modality bias issue since they involve single-modality training or clustering.

2.2. Causal Inference

Incorporating causal inference [15] into deep learning models, enabling them to learn causal effects, can enhance the performance across various applications [16]. There has been research exploring the integration of causal inference into person ReID models. For instance, CIFT [17] utilized counterfactual interventions and causal effect tools to make the graph topology structure more reliable for the VI-ReID graph model. Zhang *et al.*[18] approximated causal interventions on domain-specific factors to achieve domain-invariant representation learning for generalizable ReID. Both AIM [19] and CCIL [20] employed causal intervention models to learn clothing-invariant features for cloth-changing person ReID. These methods cannot be applied in the USL-VI-ReID task since they are designed to mitigate biases caused by domain and clothing rather than modality.

2.3. Learning with Noisy Labels

Learning with noisy labels has gained significant attention, as clean labels are often scarce in practice. Existing methods mitigate label noise through designing robust loss functions [21], noise-aware sample re-weighting [22], and label correction [23]. Noise label learning has been extensively incorporated into cluster-based unsupervised ReID to refine pseudo-labels and improve model stability. For example, RCLL [24] regularizes noisy pseudo-labels by smoothing their temporal variations across epochs. STDA [25] aggregates spatial-level neighborhood consistency to refine pseudo-labels, while PPLR [26] reduces label noise by integrating global and partial predictions with label smoothing. However, these methods mainly operate

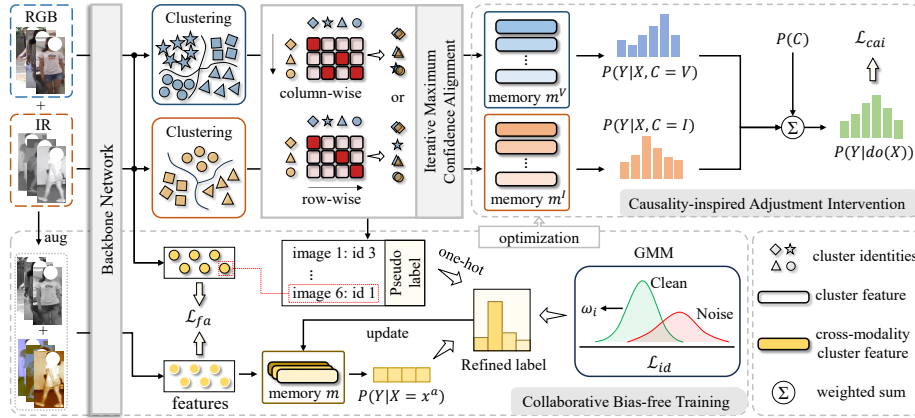


Figure 2: The framework of the proposed DMDL. After obtaining cross-modality pseudo-labels through Iterative Maximum Confidence Alignment, the Causality-inspired Adjustment Intervention module is implemented for causal modeling to construct a low-biased model. Then, the Collaborative Bias-free Training strategy combines label refinement and modality alignment with data augmentation to optimize the model, further eliminating modality bias during training.

on single-modality clustering, leveraging temporal, spatial, or fine-grained contextual cues, and thus struggle to correct erroneous cross-modality relationships. In the USL-VI-ReID task, DPIS [27] and MMM [28] incorporate noisy-label learning by fitting a two-component Gaussian Mixture Model (GMM) to the loss distribution to estimate label confidence, which is then used to penalize noisy samples during optimization. In contrast to such penalization-based strategies, we exploit the estimated confidence to explicitly revise pseudo-labels, thereby mitigating modality bias at the label level rather than merely suppressing its effect.

3. Proposed Method

3.1. Overview

The framework of Dual-level Modality Debiasing Learning (DMDL) is shown in Fig. 2, incorporating the Causality-inspired Adjustment Intervention (CAI) module and the Collaborative Bias-free Training (CBT) strategy. In cross-modality learning, DMDL first iteratively matches clusters across different modalities to obtain cross-modality relationships as a kind of pseudo-label. Then, CAI employs a backdoor ad-

justment algorithm to implement causal intervention, which guides the model to capture causal patterns, resulting in a low-biased model. Furthermore, to avoid misleading optimization caused by biased cues, CBT incorporates label refinement and feature alignment with modality-specific data augmentation to jointly mitigate modality bias across different levels. This methodology leads to modality-invariant features and a more generalized model.

3.2. Baseline for Two-stage USL-VI-ReID

To better illustrate the design of our method and facilitate the organization of experiments, we construct a baseline for two-stage USL-VI-ReID regarding previous works [3, 4], which contains a single-modality pre-training stage and a cross-modality learning stage.

The first single-modality learning stage is operated in a clustering-based unsupervised learning manner. Before each training epoch, we first perform clustering on the data from each modality and construct single-modality cluster memories, denoted as m^c , by averaging the features of each cluster. m_k^c represents the centroid of cluster k in modality $c \in \{V, I\}$, where V means visible and I is infrared. Then, we train the model by contrastive learning on the memory center and corresponding data as follows:

$$\mathcal{L}_{id}^c = -\log \frac{\exp(f_x^c \cdot m_+^c / \sigma)}{\sum_k \exp(f_x^c \cdot m_k^c / \sigma)}, \quad (1)$$

where f_x^c is the feature of the image x with the modality c , m_+ is the positive cluster representation, and σ is a temperature hyper-parameter. The single-modality model is trained with $\mathcal{L}_{id}^V + \mathcal{L}_{id}^I + \lambda_{tri} \cdot \mathcal{L}_{tri}$, where \mathcal{L}_{tri} is the triplet loss [29], and λ_{tri} controls the weight of \mathcal{L}_{tri} which dynamically changes during training.

In the second stage, we initialize cross-modality learning using the pretrained single-modality model and adopt the clustering-based unsupervised learning pipeline. To obtain cross-modality pseudo-labels, we propose a simple yet effective **Iterative Maximum Confidence Alignment (iMCA)** scheme in the baseline to quickly match the N clusters of one modality with the M clusters of the other. Let the modality with N clusters be denoted as C_N and the other with M clusters as C_M . iMCA first calculates

the cosine similarity between cluster centroids to construct an $N \times M$ similarity matrix S , where $S_{i,j}$ represents the similarity between the i -th cluster of C_N and the j -th cluster of C_M . With this, we perform two ways of matching: row-wise and column-wise. In the row-wise matching, for the i -th row of S , we find its matched cluster index $u_i^{row} \in [0, M]$ as follows:

$$u_i^{row} = \arg \max_j S_{i,j}. \quad (2)$$

The pseudo-label of the u_i^{row} -th cluster in C_M is then assigned to the i -th cluster in C_N . This operation is applied to all rows ($\forall i \in [0, N]$), effectively propagating labels from C_M to C_N . In the column-wise matching, the same procedure is performed for all columns to propagate labels from C_N to C_M . By alternating between row-wise and column-wise matchings across different epochs, iMCA obtains cross-modality pseudo-labels while preventing the model from being overconfident in a certain matching. Then, cross-modality cluster memories m_k are established based on unified cross-modality labels for contrastive learning as follows:

$$\mathcal{L}_{id} = -\log \frac{\exp(f_x \cdot m_+ / \sigma)}{\sum_k \exp(f_x \cdot m_k / \sigma)}. \quad (3)$$

Finally, the unsupervised cross-modality model is trained with $\mathcal{L}_{id} + \lambda_{tri} \cdot \mathcal{L}_{tri}$.

3.3. Modeling with Causal Intervention

In this section, we first consider USL-VI-ReID from the causal view, analyzing that spurious bias patterns are captured by traditional likelihood-based modeling through a backdoor, whereas causal intervention is not. Based on this analysis, we then illustrate the causal modeling in the proposed CAI module, which constructs a cross-modality model that is insensitive to modality bias.

3.3.1. USL-VI-ReID from Causal View

To illustrate our motivation for modality debiasing from the causal view, we represent the cross-modality learning process of USL-VI-ReID into the Structural Causal Model (SCM) framework [15], as shown in Fig. 3 (a). The SCM depicts the relationships among the variables ‘images’ X , ‘labels’ Y , and ‘modalities’ C . The arrow $C \rightarrow X$ indicates that the modality determines the image pixel values. $C \rightarrow Y$ reflects

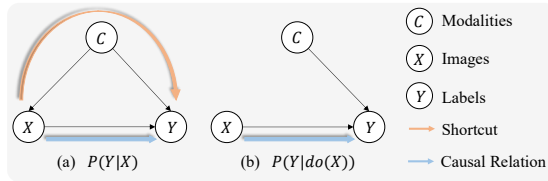


Figure 3: (a) The structural causal model in cross-modality learning for USL-VI-ReID. (b) The modified structural causal model after the causal intervention.

the modality bias issue, resulting in biased labels in cross-modality learning. $X \rightarrow Y$ means causal relationships that can recognize human identity from given images.

From this view, we can find that the modality bias $C \rightarrow Y$ establishes a backdoor from X to Y , written as $X \leftarrow C \rightarrow Y$. This backdoor path implies a shortcut for inferring the label by utilizing modality-specific information extracted from the image. This shortcut is entangled with the causal relationship and inevitably captured by the likelihood model $P(Y|X)$, which directly models all relationships between X and Y .

We utilize causal intervention to tackle this problem, as shown in Fig. 3 (b). The intervention probability $P(Y|do(X = x))$ means inferring the label conditioned on the intervened image X as a specific input x . The intervention operation $do(\cdot)$ means X is independent of all its potential causes, so $C \rightarrow X$ has also been blocked, thereby blocking the backdoor. As a result, the model infers identities directly from images rather than modality-specific cues, eliminating the modality bias and leading to generalized results. This inspires us to implement intervention in CAI, preventing the model from learning modality bias via the backdoor.

3.3.2. Causality-inspired Adjustment Intervention

Based on the above analysis, an intervention loss L_{cai} is constructed by maximizing the intervention probability to eliminate the interference of the modality bias:

$$\mathcal{L}_{cai} = \mathbb{E}_{x,y}[-\log P(Y = y|do(X = x))]. \quad (4)$$

To achieve that, CAI implements the computation of $P(Y|do(X))$ by backdoor adjustment [15] (the detailed derivation is provided in Appendix A), as follows:

$$P(Y|do(X)) = \sum_{c \in \{V,I\}} P(Y|X, C = c) \cdot P(C = c), \quad (5)$$

where $P(C = c)$ means the probabilities of modality c , and can be approximated from the training set. $P(Y|X = x, C = c)$ represents the classification probability of a specific image x inferred by incorporating specific knowledge of modality c . Importantly, c is not the modality of x , which means that the inference needs to combine the image with both two modality-specific knowledge. We achieve this by using single-modality memories as follows:

$$P(Y = y|X = x, C = c) = \frac{\exp(f_x \cdot m_y^c / \sigma)}{\sum_k \exp(f_x \cdot m_k^c / \sigma)}, \quad (6)$$

where f_x is the feature extracted by the backbone model, y represents the cross-modality pseudo-label of the image x , and m_y^c is the cluster centroid of y -th cluster of modality c . With these modeled probability parts, we can train the model following Eq. (4).

We provide further analysis of CAI. Compared to the likelihood model $P(Y|X)$ which can be decomposed as follows:

$$P(Y|X) = \sum_c P(Y|X, C = c) \cdot P(C = c|X), \quad (7)$$

the backdoor adjustment modifies $P(C = c|X)$ to $P(C = c)$, which can be seen as blocking the correlation between modalities C and images X . It eliminates the modality bias during modeling, achieving a low-biased cross-modality model by capturing purely causal relationships.

3.4. Collaborative Bias-free Training

Although a low-biased model is obtained through CAI, the biased modality-specific cues existing in labels and features still mislead the model training. To tackle this problem, we propose the CBT strategy to mitigate modality bias at the optimization level. Specifically, considering that modality bias propagates from data into labels and features, CBT integrates label refinement and feature alignment with well-designed data augmentation, thereby disrupting bias propagation and promoting unbiased feature learning.

3.4.1. Data Augmentation in CBT

CBT first introduces a modality-specific augmentation scheme to destroy modality-related information in images, as shown in Fig. 4. Specifically, for infrared images,

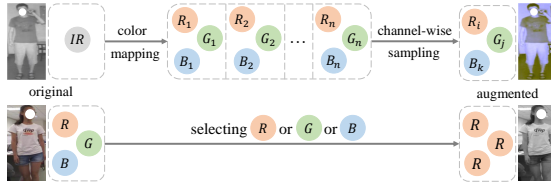


Figure 4: Illustration of the modality-specific augmentation. Circles represent channels of images. Subscript represents the sample index of pseudo-color images. For example, R_2 , G_2 , and B_2 are the red, green, and blue channels from the same pseudo-color image with index 2. The grey circle with IR indicates the single channel of the infrared image.

we first employ a series of color mapping methods to transfer each infrared image to multiple pseudo-color images. Then, a channel-wise sampling scheme is proposed to increase diversity and introduce randomness to the augmentation by randomly sampling R, G, and B channels of multiple generated pseudo-color images and combining the corresponding sampled channels into a new image. For visible images, we employ channel augmentation (CA) [1] through channel multiplexing to generate augmented images, which could derive a series of augmented samples that look like infrared.

This modality-specific data augmentation enables the image and its corresponding augmentation to share the same identity-discriminative information but differ in modality-related information, mitigating the modality bias at the data level. With the assistance of such augmentation, CBT implements label refinement and feature alignment to facilitate bias-free learning.

3.4.2. Label Refinement in CBT

To refine the noise pseudo-labels, CBT employs label smoothing by exchanging the predictions of images and their augmented images as follows:

$$\begin{cases} \tilde{\mathbf{y}}_i = w_i \mathbf{y}_i + (1 - w_i) P(Y|X = x_i^a) \\ \tilde{\mathbf{y}}_i^a = w_i \mathbf{y}_i + (1 - w_i) P(Y|X = x_i), \end{cases} \quad (8)$$

where boldface \mathbf{y}_i means the one-hot label vector in which the ground-truth class y_i index is set to 1 and others are 0. $\tilde{\mathbf{y}}_i$ and $\tilde{\mathbf{y}}_i^a$ represent the refined label vectors of image x_i and its augmentation x_i^a , respectively. Then, they are used to supervise the model

training by modifying the \mathcal{L}_{cai} in Eq. (4) as soft-label classification loss as follows:

$$\begin{aligned} \mathcal{L}_{cai} = \mathbb{E}_i[& - \sum_k \tilde{\mathbf{y}}_i[k] \cdot \log P(Y = k | do(X = x_i)) \\ & - \sum_k \tilde{\mathbf{y}}_i^a[k] \cdot \log P(Y = k | do(X = x_i^a))], \end{aligned} \quad (9)$$

where $\tilde{\mathbf{y}}_i[k]$ means index k -th value of $\tilde{\mathbf{y}}_i$. The computations of $\tilde{\mathbf{y}}$ and $\tilde{\mathbf{y}}^a$ depend on w_i and $P(Y|X)$, where the former is the certainty of y_i , and the latter is the likelihood function.

Refer to Eq. (8), the certainty w_i reflects the reliability of the label for the i -th sample. A higher w_i indicates a higher-quality label, allowing y_i to contribute more significantly than $P(Y|X)$ to the final refined label. To quantify the reliability of each label y_i as w_i , we follow a common practice in noise label learning [30] by modeling the distribution of sample losses using a Gaussian Mixture Model (GMM). Specifically, we first compute the loss value for each sample via cross-entropy:

$$\mathcal{L}_{id}^i = -\log P(Y = y_i | X = x_i). \quad (10)$$

The overall loss distribution \mathcal{L}_{id} is then fitted with a two-component GMM, where one component corresponds to low-loss samples (indicating high-quality labels) and the other to high-loss samples (indicating low-quality labels). After training, the GMM estimates the probability that a given loss \mathcal{L}_{id}^i belongs to the low-loss component, which is used as the label certainty w_i .

Note that $P(Y|X)$ plays a crucial role in computing both the certainty and the refined labels. We follow Eq. (7) to implement $P(Y|X)$ but adopt Normalized Weighted Geometric Mean (NWGM) [31] for simplification (details are provided in Appendix B). In one word, $P(Y|X)$ is computed using the modality-shared memory features m :

$$P(Y = y | X = x) = \frac{\exp(f_x \cdot m_y / \sigma)}{\sum_k \exp(f_x \cdot m_k / \sigma)}. \quad (11)$$

It is evident that the quality of the memory bank directly influences the reliability of the predictions. To enhance prediction robustness, we design a dynamic updating scheme that iteratively updates the memory features:

$$m_y \leftarrow \eta_x m_y + (1 - \eta_x) f_x, \quad (12)$$

where η_x is an adaptive coefficient determined by:

$$\eta_x = \eta / \max(\tilde{\mathbf{y}}_x[k == y], \eta). \quad (13)$$

Here, $\tilde{\mathbf{y}}_x[k == y]$ denotes the refined label confidence of sample x for class y , and η is a constant threshold set to 0.2. This adaptive coefficient ensures that samples with higher label confidence contribute more substantially to updating the corresponding memory feature m_y , while low-confidence samples have limited influence.

Compared with methods [27, 28] that only penalize noisy samples based on label certainty, the proposed label refinement directly constructs low-biased cross-modality labels by incorporating modality-specific augmentations and dynamically updating the modality-shared memory. Since an image and its modality-specific augmentation contain different modality-related information, exchanging their predictions for label smoothing effectively reduces label noise induced by modality-specific cues. Furthermore, the dynamic memory updating scheme prevents the memory bank from accumulating noisy representations, thereby ensuring more reliable predictions for refining labels.

3.4.3. Feature Alignment in CBT

In addition, a feature alignment loss is introduced to further enhance bias-free feature learning. It is well understood that identity-discriminative information should remain consistent under augmentation. Therefore, for an image and its modality-specific augmentation, the model is expected to extract similar features; otherwise, it suggests that the model is learning modality-specific knowledge. To this end, we design \mathcal{L}_{fa} following the principles of MMD [32]:

$$\mathcal{L}_{fa} = \sum_{c \in \{V, I\}} \left\| \frac{1}{n} \sum_{i=1}^n \phi(f_i^c) - \frac{1}{n} \sum_{i=1}^n \phi(f_i^{ca}) \right\|_{\mathcal{H}}^2, \quad (14)$$

where f_i^{ca} represents the features of the augmented images of modality c . $\|\cdot\|_{\mathcal{H}}$ denotes the distance measured by the Gaussian kernel function $\phi(\cdot)$, which maps the input to the Reproducing Kernel Hilbert Space (RKHS). This loss constrains the original image and its augmentation representations to be close in the metric space, thereby mitigating the modality-specific cues learned in feature representations.

3.5. Total Loss of DMDL

Following the baseline, the total loss function of our DMDL can be written as:

$$\mathcal{L} = \mathcal{L}_{id}^V + \mathcal{L}_{id}^I + \lambda_{cai} \cdot \mathcal{L}_{cai} + \lambda_{fa} \cdot \mathcal{L}_{fa} + \lambda_{tri} \cdot \mathcal{L}_{tri}, \quad (15)$$

where λ_{cai} , λ_{fa} and λ_{tri} are weights of the corresponding loss term.

4. Experiments

4.1. Datasets and Evaluation Protocol

Dataset. In this section, we conduct comprehensive experiments to evaluate the proposed method on two widely used datasets, SYSU-MM01 [33] and RegDB [34], as well as a more recent dataset, LLCM [35].

The *SYSU-MM01* dataset with 4 visible cameras and 2 infrared cameras, capturing 395 identities for training and 96 for testing. The test query set comprises 3,803 infrared images, and the gallery set contains 301 visible images. The evaluation protocol provides all-search and indoor-search modes.

The *RegDB* is a dual-camera dataset with 412 identities, each having 10 visible and 10 infrared images. It is split into 206 identities for training and 206 for testing. The evaluation protocol includes two test modes: visible to infrared and infrared to visible.

The *LLCM* is the largest VI-ReID dataset that captures images with 9 cameras. It contains 1,064 identities, of which 713 are used for training and 351 for testing. The evaluation protocol includes two test modes: VIS to IR and IR to VIS.

Evaluation protocol. All experiments follow the standard evaluation protocol in the VI-ReID benchmark testing. Our model is evaluated using different training/testing splits in ten trials to ensure stable performance. Evaluation metrics include cumulative matching characteristics (CMC), mean average precision (mAP), and mean inverse negative penalty (mINP) [36].

4.2. Implementation Details

We employ ResNet-50 pre-trained on ImageNet as the backbone network and integrate Non-local Attention Blocks [37] and generalized-mean (GeM) pooling [38].

During training, 16 identities are sampled from each modality, with 16 instances per identity. All input images are resized to 288×144 , and standard data augmentation techniques, including horizontal flipping, random cropping, and random erasing, are applied. The model is optimized using Adam with an initial learning rate of 3.5×10^{-4} and a weight decay of 5×10^{-4} . The learning rate is decreased by a factor of ten every 20 epochs. The hyperparameter σ is set to 0.05. Training proceeds for a total of 100 epochs, with the first 50 epochs dedicated to single-modality learning, followed by 50 epochs of cross-modality training.

4.3. Comparison with State-of-the-art Methods

To validate the effectiveness of our DMDL, we compare it with state-of-the-art methods under three relevant settings: supervised VI-ReID, semi-supervised VI-ReID, and unsupervised VI-ReID. The experimental results for the SYSU-MM01 and RegDB datasets are shown in Table 1, and the experimental results for the LLCM dataset are presented in Table 2.

Comparison with supervised VI-ReID Methods. Encouragingly, our DMDL achieves competitive performance compared to the supervised method FMCNet [40] on the SYSU-MM01 and RegDB datasets, and even surpasses several supervised methods, including AGW [36] and SPOT [39]. Moreover, on the challenging LLCM dataset, our DMDL still demonstrates impressive performance, outperforming several supervised methods (e.g., AGW [36] and LbA [48]). However, due to the absence of annotated cross-modality correspondences, unsupervised methods still have significant room for improvement compared to the state-of-the-art supervised VI-ReID methods.

Comparison with semi-supervised VI-ReID Methods. Semi-supervised VI-ReID methods are trained on datasets with partial annotations. Remarkably, our DMDL achieves outstanding performance without relying on any annotations, surpassing all semi-supervised counterparts, as reported in Table 1. These results highlight the potential of USL-VI-ReID, which eliminates the need for annotations and offers greater practicality.

Comparison with unsupervised VI-ReID Methods. The results in Table 1 demonstrate that our method achieves superior performance under the unsupervised VI-ReID

Methods	Venue	SYSU-MM01						RegDB					
		All Search			Indoor Search			Visible to Infrared			Infrared to Visible		
		r1	mAP	mINP	r1	mAP	mINP	r1	mAP	mINP	r1	mAP	mINP
<i>Supervised VI-ReID methods</i>													
AGW [36]	TPAMI-21	47.50	47.65	35.30	54.17	62.97	59.23	70.05	66.37	50.19	70.49	65.90	51.24
CA [1]	ICCV-21	69.88	66.89	53.61	76.26	80.37	76.79	85.03	79.14	65.33	84.75	77.82	61.56
SPOT [39]	TIP-22	65.34	62.25	-	69.42	74.63	-	80.35	72.46	-	79.37	72.26	-
FMCNet [40]	CVPR-22	66.34	62.51	-	68.15	74.09	-	89.12	84.43	-	88.38	83.86	-
MUN [41]	ICCV-23	76.24	73.81	-	79.42	82.06	-	95.19	87.15	-	91.86	85.01	-
IDKL [2]	CVPR-24	81.42	79.85	-	87.14	89.37	-	94.72	90.19	-	94.22	90.43	-
TSKD [42]	PR-25	76.6	73.0	-	82.7	85.3	-	91.1	81.7	-	89.9	80.5	-
<i>Semi-supervised VI-ReID methods</i>													
OTLA [43]	ECCV-22	48.2	43.9	-	47.4	56.8	-	49.9	41.8	-	49.6	42.8	-
DPIS [27]	ICCV-23	58.4	55.6	-	63.0	70.0	-	62.3	53.2	-	61.5	52.7	-
CGSFL [44]	PR-25	59.83	53.12	35.79	61.50	63.83	60.66	89.36	84.17	69.47	89.11	81.49	66.43
<i>Unsupervised VI-ReID methods</i>													
ADCA [3]	MM-22	45.51	42.73	28.29	50.60	59.11	55.17	67.20	64.05	52.67	68.48	63.81	49.62
DOTLA [9]	MM-23	50.36	47.36	32.40	53.47	61.73	57.35	85.63	76.71	61.58	82.91	74.97	58.60
MBCCM [5]	MM-23	53.14	48.16	32.41	55.21	61.98	57.13	83.79	77.87	65.04	82.82	76.74	61.73
PGM [4]	CVPR-23	57.27	51.78	34.96	56.23	62.74	58.13	69.48	65.41	52.97	69.85	65.17	-
CHCR [13]	TCSVT-23	59.47	59.14	-	-	-	-	69.31	64.74	-	69.96	65.87	-
GUR* [12]	ICCV-23	63.51	61.63	47.93	71.11	76.23	72.57	73.91	70.23	58.88	75.00	69.94	56.21
MMM [28]	ECCV-24	61.6	57.9	-	64.4	70.4	-	89.7	80.5	-	85.8	77.0	-
PCLHD [6]	NIPS-24	64.4	58.7	-	69.5	74.4	-	84.3	80.7	-	82.7	78.4	-
SDCL [†] [14]	CVPR-24	64.49	63.24	51.06	71.37	76.90	73.50	86.91	78.92	62.83	85.76	77.25	59.57
MULT [10]	IJCV-24	64.77	59.23	43.46	65.34	71.46	67.83	89.95	82.09	67.29	90.78	82.25	65.38
PCAL [45]	TIFS-25	57.94	52.85	36.90	60.07	66.73	62.09	86.43	82.51	72.33	86.21	81.23	68.71
N-ULC [7]	AAAI-25	61.81	58.92	45.01	67.04	73.08	69.42	88.75	82.14	68.75	88.17	81.11	66.05
DLM [11]	TPAMI-25	62.15	58.42	43.70	67.31	72.86	68.89	87.55	82.83	71.93	86.84	81.94	68.96
RoDE [46]	TIFS-25	62.88	57.91	43.04	64.53	70.42	66.04	88.77	78.98	67.99	85.78	78.43	62.34
SALCR [47]	IJCV-25	64.44	60.44	45.19	67.17	72.88	68.73	90.58	83.87	70.76	88.69	82.66	66.89
DMDL	Ours	65.90	61.86	47.53	70.66	75.45	71.66	90.63	85.33	73.79	90.30	85.04	72.00
DMDL*	Ours	68.04	65.42	52.01	74.81	79.42	76.13	-	-	-	-	-	-

Table 1: Comparison with the state-of-the-art methods on SYSU-MM01 and RegDB. Rank at r accuracy(%), mAP (%) and mINP (%) are reported. * denotes the results of training with extra camera information. † indicates that the method is initialized with a ReID model pre-trained on additional ReID datasets. The best results are in **bold**.

setting. Specifically, DMDL attains 65.42% mAP on SYSU-MM01 (all-search) and 85.33% mAP on RegDB (visible-to-infrared), outperforming the latest method SALCR [47] by 4.98% and 1.46% mAP on the respective datasets. Notably, even without utilizing camera information, our approach still achieves 65.90% rank-1 accuracy and 61.86% mAP on SYSU-MM01 (all-search), surpassing existing methods except SDCL [14].

Methods	Venue	LLCM					
		IR to VIS			VIS to IR		
		r1	mAP	mINP	r1	mAP	mINP
<i>Supervised VI-ReID methods</i>							
AGW [36]	TPAMI-21	43.6	51.8	-	51.5	55.3	-
LbA [48]	ICCV-21	43.8	53.1	-	50.8	55.6	-
CA [1]	ICCV-21	48.8	56.6	-	56.5	59.8	-
DART [49]	CVPR-22	52.2	59.8	-	60.4	63.2	-
DEEN [35]	CVPR-23	54.9	62.9	-	62.5	65.8	-
CM ² GT [50]	PR-25	52.1	58.3	-	65.9	50.3	-
<i>Unsupervised VI-ReID methods</i>							
ADCA [3]	MM-22	23.57	28.25	-	16.16	21.48	-
DOTLA [9]	MM-23	27.14	26.26	-	23.52	27.48	-
GUR [12]	ICCV-23	31.47	34.77	-	29.68	33.38	-
IMSL [51]	TCSVT-24	22.74	19.38	-	17.26	24.38	-
RoDE [46]	TIFS-25	32.73	36.64	-	35.13	37.44	-
DMDL	Ours	45.25	50.87	47.14	51.84	55.35	49.85

Table 2: Comparison with the state-of-the-art methods on the LLCM dataset. Rank at r accuracy(%), mAP (%) and mINP (%) are reported. The best results are in **bold**.

However, SDCL is initialized with a model pre-trained on external ReID datasets, which provides it with an unfair advantage in comparison. Meanwhile, on the more challenging LLCM dataset, our method showcases remarkable performance, surpassing the state-of-the-art RoDE [46] by 14.23% mAP and 12.52% rank-1 accuracy in the IR to VIS setting, as reported in Table 2.

These results suggest that while existing methods have made notable progress on the USL-VI-ReID task, they still suffer from modality bias, leading to the extraction of modality-dependent features. In contrast, our DMDL effectively learns modality-invariant representations by addressing modality bias through causal modeling and bias-free training optimization, achieving more robust performance.

4.4. Ablation Study

To evaluate the contribution of each component in DMDL, we conduct ablation experiments on the SYSU-MM01 dataset, as summarized in Table 3. Note that channel

Index	Components					SYSU-MM01									
	Baseline	CAI	CBT			All Search					Indoor Search				
			data	label	feature	r1	r5	r10	mAP	mINP	r1	r5	r10	mAP	mINP
1	✓					56.26	84.12	92.19	54.60	40.75	63.98	87.77	94.06	69.68	65.30
2	✓	✓				59.61	85.34	92.94	57.85	44.31	67.07	89.67	95.02	72.94	69.00
3	✓	✓	✓			62.17	87.01	93.82	58.76	45.59	68.07	89.92	94.51	73.08	69.25
4	✓	✓	✓	✓		63.11	87.67	94.66	59.61	45.34	68.34	90.22	95.29	73.06	69.09
5	✓	✓	✓		✓	64.09	88.07	94.65	61.19	47.41	68.56	90.36	95.27	73.91	70.08
6	✓		✓	✓	✓	63.39	87.88	93.85	59.78	45.08	67.26	90.31	95.52	72.77	68.44
7	✓	✓	✓	✓	✓	65.90	88.56	94.71	61.86	47.53	70.66	91.18	95.78	75.45	71.66

Table 3: Ablation studies on the SYSU-MM01. Rank at r accuracy (%), mAP (%) and mINP (%) are reported.

augmentation (CA) [1] for visible images is incorporated into the *baseline* to ensure a fair assessment of our designed components.

Effectiveness of CAI. When CAI is applied by replacing traditional likelihood-based modeling in *baseline* with causal modeling, the rank-1 accuracy and mAP of all-search increase by 3.35% and 3.25%, respectively (Index 1 vs. 2). This demonstrates that CAI effectively constructs a low-biased model by explicitly modeling causal relationships between images and labels, enhancing the model’s robustness to modality variation.

Discussion of removing CAI. We conduct the experiments of removing CAI and only using CBT with baseline (Index 6). Compared with the full DMDL (CAI+CBT), using CBT alone degrades the rank-1 accuracy by approximately 2–3%, suggesting that CAI and CBT are most effective when used jointly. CAI constructs a low-biased model, while CBT suppresses the injection of biased cues into the model during optimization. They act on the complementary modeling and optimization stages, and reinforce each other in modality debiasing.

Effectiveness of CBT. Compared with the results in Index 2, the experiments in Index 7 show that the proposed optimization strategy, CBT, achieves a 6.29% improvement in rank-1 accuracy (all-search), confirming its effectiveness in bias-free feature learning. Specifically, CBT comprises three components: data augmentation, label refinement, and feature alignment. When integrated sequentially, these components yield consistent performance gains (Index 3–7). This trend indicates that each component mitigates modality bias at different levels, contributes to learn modality-invariant representations,

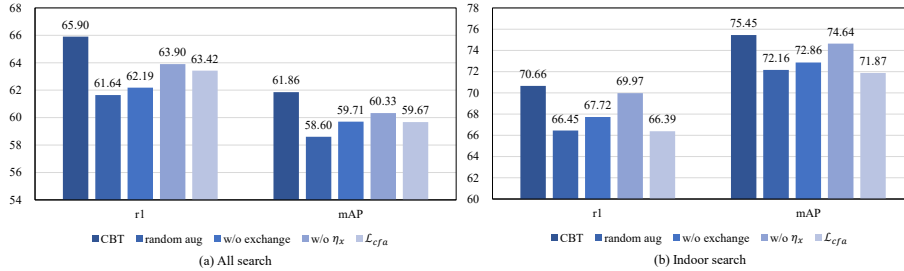


Figure 5: Detailed analysis of CBT on the SYSU-MM01 dataset under (a) all-search and (b) indoor-search modes. Rank-1 accuracy (%) and mAP (%) are reported.

and produces a mutually reinforcing effect. Below, we present a detailed analysis of these components in CBT.

Effectiveness of data augmentation in CBT. To verify the effectiveness of modality-specific augmentation, we replace it with standard random augmentation schemes (e.g., random cropping) within the CBT strategy. As shown in the second column “random aug” of Fig. 5, this replacement results in a drop of about 4% in rank-1 accuracy. This drop indicates that modality-specific augmentation plays a crucial role in CBT, as it explicitly disrupts modality-specific information in the images and thus guides the model to learn modality-shared representations. Moreover, when only the modality-specific augmentation is applied, the model still achieves an overall performance improvement (Index 3 vs. 4), further demonstrating that this augmentation effectively mitigates modality bias at the data level.

Effectiveness of label refinement in CBT. Based on the data augmentation, the label refinement scheme introduces two key designs: (1) exchanging predictions between an image and its augmentation, and (2) dynamically updating the memory with adaptive η_x . To evaluate the effectiveness of these designs, we conduct ablation experiments under the “w/o exchange” and “w/o η_x ” settings, the results of which are shown in the third and fourth columns of Fig. 5. Specifically, the “w/o exchange” variant refines the pseudo-label using its own prediction rather than that of its augmentation, while the “w/o η_x ” variant fixes $\eta = 0.05$ for memory updating. Both variants lead to performance degradation, confirming that: (1) exchanging predictions between images and

their modality-specific augmentations mitigates modality bias in refined labels, as the augmentation perturbs modality-specific cues, yielding less biased predictions for refining labels, and (2) dynamic updating enhances memory reliability, enabling stable predictions. By integrating these two designs, CBT effectively mitigates modality bias at the label level, resulting in a substantial performance improvement (Index 3 vs. 4).

Effectiveness of feature alignment in CBT. We observe a notable performance gain after incorporating the feature alignment loss \mathcal{L}_{fa} into CBT (Index 3 vs. 5), indicating that \mathcal{L}_{fa} effectively alleviates modality bias in feature representations by aligning images and their augmentation. To further validate the effectiveness of our design, we replace \mathcal{L}_{fa} with an MMD-based loss \mathcal{L}_{cfa} commonly adopted in conventional VI-ReID methods, which enforces direct alignment between visible and infrared feature distributions to reduce modality gap:

$$\mathcal{L}_{cfa} = \left\| \frac{1}{n} \sum_{i=1}^n \phi(f_i^V) - \frac{1}{n} \sum_{i=1}^n \phi(f_i^I) \right\|_{\mathcal{H}}^2. \quad (16)$$

As shown in the fifth column of Fig. 5, \mathcal{L}_{cfa} results in degraded performance, since inconsistent cross-modality pseudo-labels lead to identity misalignment and weaken feature discriminability. In contrast, \mathcal{L}_{fa} leverages the natural correspondence between original and augmented images, aligning modalities in a label-consistent and feature-discriminative manner. Furthermore, combining augmentation-based label refinement and feature alignment achieves the best result (Index 7), indicating that CBT effectively promotes bias-free feature learning by interrupting the propagation of modality bias across data, labels, and features.

4.5. Further Analysis

Parameter Analysis. The proposed DMDL introduces two key parameters, λ_{cai} and λ_{fa} in Eq. 15, which serve as weighting factors to balance \mathcal{L}_{cai} and \mathcal{L}_{fa} during training. Fig. 6 (a) illustrates the impact of varying λ_{cai} on rank-1 and mAP accuracy on the SYSU-MM01 dataset (all-search). When $\lambda_{cai} = 0$, the CAI is disabled, resulting in poor performance, which confirms its effectiveness. The best performance is observed at $\lambda_{cai} = 0.5$, and this value is therefore adopted in our experiments. Fig. 6

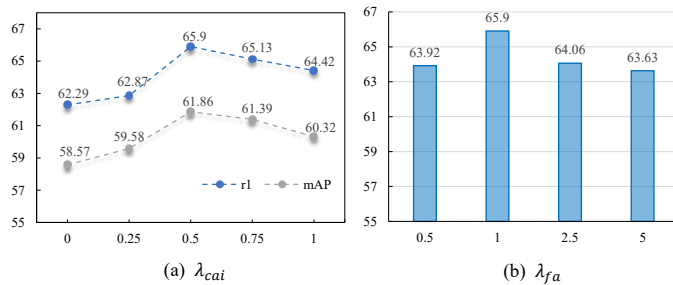


Figure 6: Parameter analysis of λ_{cai} and λ_{fa} on the SYSU-MM01 dataset (all-search).

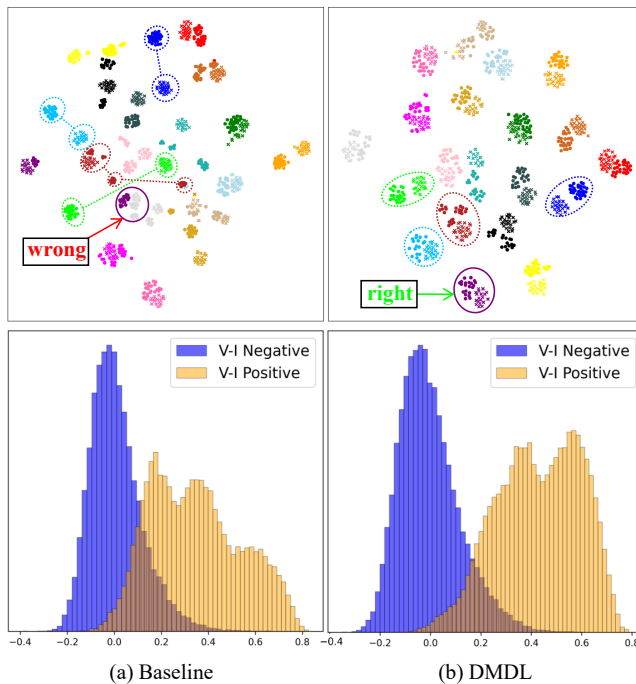


Figure 7: The t-SNE (first row) and similarity distribution (second row) visualization of 20 randomly selected identities on the SYSU-MM01 dataset. In t-SNE visualization, the circle and the cross represent the visible and infrared modalities, respectively.

(b) shows the rank-1 accuracy results for different λ_{fa} values, and the model achieves the highest accuracy at $\lambda_{fa} = 1$, so we empirically set it to 1. For completeness, the sensitivity analysis of λ_{tri} used in *baseline* is provided in Appendix C, as it is not our main contribution.

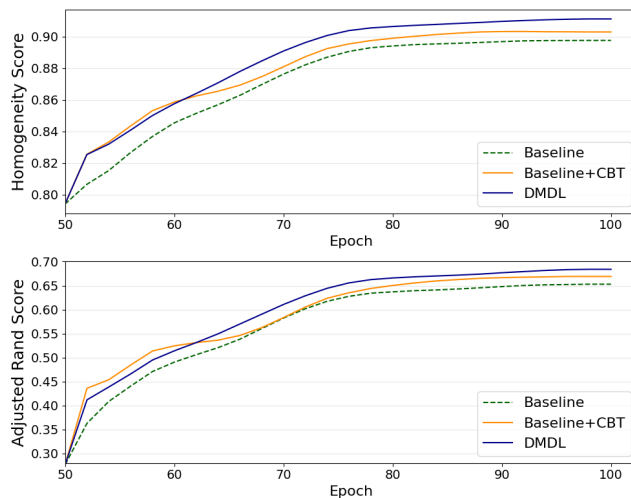


Figure 8: Cross-modality pseudo-label quality analysis over different epochs on the SYSU-MM01 dataset.

Visualization Analysis. Fig. 7 presents the t-SNE [52] plots and the cosine similarity distribution of positive and negative cross-modality pairs for randomly selected identities. Compared with the baseline, DMDL exhibits a more compact alignment between visible and infrared samples, together with a larger separation between positive and negative cross-modality pairs. In addition, the mismatched samples highlighted by the purple circle are correctly aligned after applying DMDL. Taken together, these visualizations demonstrate that DMDL effectively narrows the modality gap and improves the robustness of the learned representation against modality bias.

Cross-modality Pseudo-label Quality Analysis. We assess the quality of cross-modality pseudo-labels generated at different training epochs on the SYSU-MM01 dataset in Fig. 8, using two standard metrics from [53]: Homogeneity Score and Adjusted Rand Score, where higher scores indicate better label quality. Notably, incorporating CBT and CAI on top of the baseline consistently improves the quality of cross-modality labels across training. This demonstrates that CBT and CAI effectively mitigate modality bias in the learned representations, thereby facilitating more accurate cross-modality matching.

Retrieval Results. We qualitatively compare our DMDL with the baseline by visu-

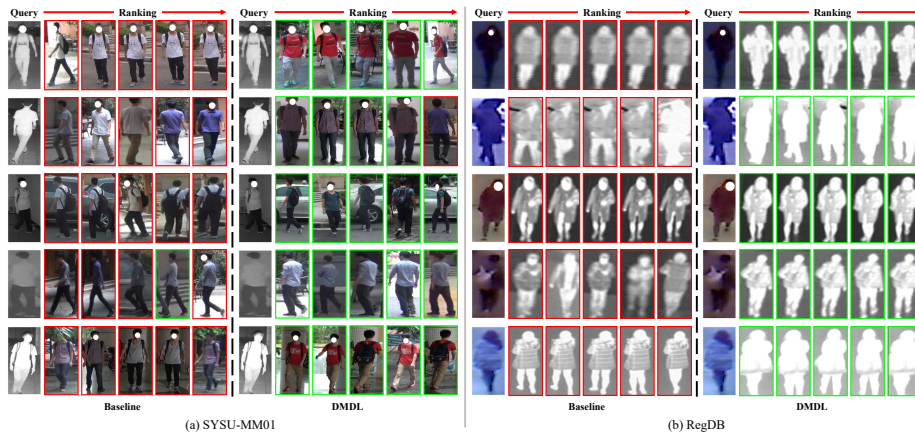


Figure 9: Visualization of the retrieval results obtained by the baseline and our DMDL on the SYSU-MM01 and RegDB datasets. The green boxes represent correct retrieval results, and the red boxes represent incorrect retrieval results.

alizing the retrieval results of several query images on SYSU-MM01 and RegDB, as illustrated in Fig. 9. For each query, the retrieved samples highlighted with green boxes indicate correct matches, while those marked in red correspond to incorrect matches. Overall, the proposed method exhibits higher robustness to modality-specific interference (e.g., color cues), whereas the baseline tends to prioritize color similarity when retrieving results (see the first row in Fig. 9). This confirms that our method achieves stronger cross-modality retrieval capability than the baseline, yielding consistent improvements.

5. Conclusion

In this paper, we investigate the modality bias issue in unsupervised VI-ReID and propose a novel Dual-level Modality Debiasing Learning (DMDL) framework to tackle this issue from both model and optimization perspectives, incorporating a Causality-inspired Adjustment Intervention (CAI) module and a Collaborative Bias-free Training (CBT) strategy. CAI models causal relationships between images and pseudo-labels to capture stable, modality-independent patterns, thereby constructing a low-biased model. Meanwhile, CBT performs label refinement and feature alignment with

modality-specific data augmentation, jointly preventing the propagation of modality bias across data, labels, and features to achieve bias-free optimization. Finally, with the above designs, DMDL effectively achieves modality-invariant feature learning. Extensive experiments on benchmark datasets validate the superior performance of our method.

Appendix A. Detail on Causal Inference

In our main paper, the Causality-inspired Adjustment Intervention (CAI) module revolves around the intervention operator $do(\cdot)$ and the computation of the interventional probability $P(Y|do(X))$. In this section, we provide further explanation and proof for these concepts.

As shown in Fig. A.1 (a), we represent the cross-modality learning process of USL-VI-ReID into the Structural Causal Model (SCM) framework [15]. It describes the causal relation between variables "images" X , "labels" Y , and confounding factor "modalities" C . We can observe that $C \rightarrow Y$ establishes a backdoor path from X to Y , written as $X \leftarrow C \rightarrow Y$. This backdoor path implies that there is a shortcut for inferring label information from the modality-specific knowledge extracted by the image. This shortcut can mislead the model to learn modality-specific cues, limiting its generalization.

To prevent the confounding influence caused by the backdoor path (i.e., shortcut) and infer the causal effect of X on Y , we implement the intervention to cut off all potential causes of X . This means that all arrows pointing towards variable X are removed, thus $X \leftarrow C$ is deleted. In this scenario, there is only the causal relation $X \rightarrow Y$ between the X and Y . The modified SCM after the causal intervention is depicted in Fig. A.1 (b). To distinguish from the original probability P , P_m represents the probability in the modified SCM, and is therefore referred to as the manipulation probability. According to the definition of intervention, $P(Y|do(X))$ is equal to the manipulation probability $P_m(Y|X)$ in the modified SCM:

$$P(Y = y|do(X = x)) = P_m(Y = y|X = x). \quad (\text{A.1})$$

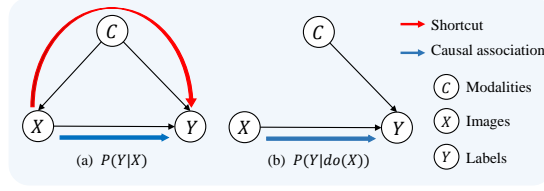


Figure A.1: (a) The structural causal model for modalities C , images X and pseudo labels Y in cross-modality learning for USL-VI-ReID. (b) The modified structural causal model after the causal intervention.

The key to estimating causal effects lies in observing the manipulation probability P_m , which possesses two fundamental properties of the original probability P . First, the marginal probability $P(C = c)$ remains unchanged after intervention, as removing the arrow from C to X does not affect the process of determining the value of C . In our task, this means that the proportions of different modalities remain unchanged before and after intervention. Second, the conditional probability $P(Y = y|X = x, C = c)$ remains invariant because the response of Y to X and C remains unchanged regardless of whether X changes spontaneously or is deliberately manipulated. Thus, two invariance equations can be given:

$$\begin{aligned}
 P_m(Y = y|X = x, C = c) &= P(Y = y|X = x, C = c), \\
 P_m(C = c) &= P(C = c).
 \end{aligned}
 \tag{A.2}$$

In addition, after implementing the intervention, X and C are independent, as shown in Fig. A.1 (b). This implies another invariance equation:

$$P_m(C = c|X = x) = P_m(C = c) = P(C = c).
 \tag{A.3}$$

In conclusion, by combining the law of total probability and the invariance relationships, we can derive the formula in CAI:

$$\begin{aligned}
P(Y = y|do(X = x)) &= P_m(Y = y|X = x) \\
&= \sum_c P_m(Y = y|X = x, C = c) \cdot P_m(C = c|X = x) \\
&= \sum_c P_m(Y = y|X = x, C = c) \cdot P_m(C = c) \\
&= \sum_c P(Y = y|X = x, C = c) \cdot P(C = c).
\end{aligned} \tag{A.4}$$

The Eq. (A.4) is a causal effect formula expressed in terms of pre-intervention probabilities. It calculates the relationship between X and Y for each value c of C and then takes the average of these values. This process is known as correction or control for C . In CAI, we can directly estimate the causal effect between X and Y from the data by applying the final form of Eq. (A.4), as it only involves pre-intervention probabilities.

Appendix B. Derivation of $P(Y|X)$

In this section, we give a derivation for simplifying $P(Y|X)$. First, the posterior probability $P(Y|X)$ could be as the marginalization over the modality variable C :

$$P(Y|X = x) = \sum_c P(Y|X = x, C = c) \cdot P(C = c|X = x), \tag{B.1}$$

where $C \in \{V, I\}$ denotes the modality (visible or infrared). The conditional term $P(Y|X = x, C = c)$ represents the classification probability for a specific image x , given the modality c . To incorporate modality-specific information, we introduce the memory representation m^c corresponding to modality c , calculating the conditional term as follows:

$$\begin{aligned}
P(Y = y|X = x, C = c) &= P(Y = y|X = x, m^c) \\
&= \text{Cls}(f_x \cdot m^c / \sigma) \\
&= \frac{\exp(f_x \cdot m_y^c / \sigma)}{\sum_k \exp(f_x \cdot m_k^c / \sigma)},
\end{aligned} \tag{B.2}$$

where f_x denotes the feature representation of image x , the classifier $\text{Cls}(\cdot)$ is a soft-max activation function, and σ is a temperature parameter that controls the distribution

sharpness. Substituting Eq. (B.2) into Eq. (B.1), we obtain:

$$P(Y|X = x) = \sum_c \text{Cls}(f_x \cdot m^c / \sigma) \cdot P(m^c|X = x), \quad (\text{B.3})$$

where $P(m^c|X = x)$ denotes the posterior weight of the memory from modality c given input x . Then, following the Normalized Weighted Geometric Mean (NWGM) approximation [31], the classifier function can be approximately moved outside the summation:

$$P(Y|X = x) \approx \text{Cls}\left(\sum_c f_x \cdot m^c \cdot P(m^c|X = x) / \sigma\right) \quad (\text{B.4})$$

We define the cross-modality memory m can be approximated as the weighted average of the modality-specific memories:

$$m = \sum_c m^c \cdot P(m^c|X = x), \quad (\text{B.5})$$

which enables us to further simplify Eq. (B.4) as:

$$\begin{aligned} P(Y|X = x) &\approx \text{Cls}\left(\sum_c f_x \cdot m / \sigma\right) \\ &= \frac{\exp(f_x \cdot m / \sigma)}{\sum_k \exp(f_x \cdot m_k / \sigma)}. \end{aligned} \quad (\text{B.6})$$

Therefore, the simplified form of $P(Y|X)$ in Eq. (B.6) is derived by approximating the marginalization over modality-specific memories through NWGM, resulting in a unified representation governed by the cross-modality memory m .

Appendix C. Analysis on Parameter

The triplet loss \mathcal{L}_{tri} is not a contribution of our method, so we implement the analysis of λ_{tri} based on the baseline. We design a dynamically changing weight for \mathcal{L}_{tri} that varies with the training epoch as follows:

$$\lambda_{tri} = \begin{cases} 0 & \text{if epoch} \leq 15, \\ 0.25 & \text{if } 15 < \text{epoch} \leq 25, \\ 0.5 & \text{if } 25 < \text{epoch} \leq 35, \\ 1 & \text{else.} \end{cases} \quad (\text{C.1})$$

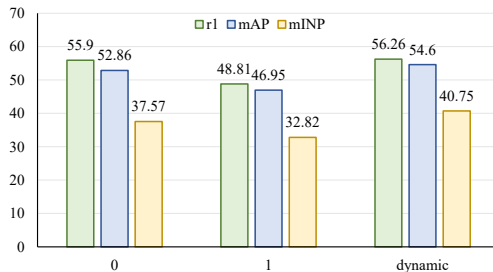


Figure C.1: Parameter analysis of λ_{tri} on the all-search mode of the SYSU-MM01 dataset.

We compare this dynamic weighting scheme with fixed weights $\lambda_{tri} = 0$ and $\lambda_{tri} = 1$, as shown in Fig. C.1. The results show that setting $\lambda_{tri} = 1$ leads to a significant performance drop compared to $\lambda_{tri} = 0$ and the dynamic scheme. This is understandable, as the pseudo-labels obtained during the early stage of unsupervised training are unreliable. Applying the triplet loss directly in the early stage may incorrectly pull samples of different identities closer, ultimately harming model performance. Furthermore, we observe that the simple dynamic weighting scheme can improve the baseline performance, and thus, it is adopted in our experiments.

Appendix D. Training with Extra Camera Information

To further enhance performance, additional camera information can be utilized to obtain more reliable clustering results to assist unsupervised training. We follow GUR [12] to replace the original features with inter-camera similarity embeddings to perform single-modality clustering, reducing the impact of camera variations on clustering.

Taking a specific modality as an example, the single-modality dataset consists of images captured by N cameras. At the beginning of each training epoch, we initially employ DBSCAN [54] to divide the data from each camera into a set of cluster centroids, denoted as $\{m_l^n\}_{l=1}^L$, where n represents the n -th camera, and L represents the number of clusters under the n -th camera. Then, for a given single-modality image x , we calculate its similarity embedding $e(x|M = n)$ under the n -th camera. The process is as follows:

$$P(Y = y|X = x, M = n) = \frac{\exp(f_x \cdot m_y^n / \sigma)}{\sum_l \exp(f_x \cdot m_l^n / \sigma)}, \quad (\text{D.1})$$

$$e(x|M = n) = [P(1|x, M = n), \dots, P(L|x, M = n)], \quad (\text{D.2})$$

where σ is a hyper-parameter, and $P(l|x, M = n)$ denotes the probability of image x at cluster l . Note that, x refers to all images in a single modality, not just the images captured by the n -th camera. We concatenate the similarity embeddings of image x from all N cameras to form inter-camera similarity embeddings:

$$E(x) = [e(x|M = 1), e(x|M = 2), \dots, e(x|M = N)]. \quad (\text{D.3})$$

We utilize $E(x)$ for clustering to obtain intra-modality pseudo labels. And inter-modality pseudo labels are obtained through the matching method iMCA. The result of training with extra camera information is presented in the experiments section of the main paper.

Discussion. GUR incorporates intra-camera clustering as an additional training stage to obtain camera-invariant representations, followed by intra-modality clustering training. We believe that intra-camera features inherently exhibit minimal non-identity differences, and their clustering results have high confidence without training. Therefore, we directly utilize the clustering results of inter-camera similarity embeddings for single-modality training. By integrating this operation, we simplify the training process while achieving high-quality clustering results.

References

- [1] M. Ye, W. Ruan, B. Du, M. Z. Shou, Channel augmented joint learning for visible-infrared recognition, in: Proceedings of the IEEE/CVF International Conference on Computer Vision, 2021, pp. 13567–13576.
- [2] K. Ren, L. Zhang, Implicit discriminative knowledge learning for visible-infrared person re-identification, in: Proceedings of the IEEE/CVF Conference on Computer Vision and Pattern Recognition, 2024, pp. 393–402.

- [3] B. Yang, M. Ye, J. Chen, Z. Wu, Augmented dual-contrastive aggregation learning for unsupervised visible-infrared person re-identification, in: Proceedings of the 30th ACM International Conference on Multimedia, 2022, pp. 2843–2851.
- [4] Z. Wu, M. Ye, Unsupervised visible-infrared person re-identification via progressive graph matching and alternate learning, in: Proceedings of the IEEE/CVF Conference on Computer Vision and Pattern Recognition, 2023, pp. 9548–9558.
- [5] D. Cheng, L. He, N. Wang, S. Zhang, Z. Wang, X. Gao, Efficient bilateral cross-modality cluster matching for unsupervised visible-infrared person reid, in: Proceedings of the 31st ACM International Conference on Multimedia, 2023, pp. 1325–1333.
- [6] J. Shi, X. Yin, Y. Zhang, Y. Xie, Y. Qu, et al., Learning commonality, divergence and variety for unsupervised visible-infrared person re-identification, *Advances in Neural Information Processing Systems* 37 (2024) 99715–99734.
- [7] X. Teng, L. Lan, D. Chen, K. Xu, N. Yin, Relieving universal label noise for unsupervised visible-infrared person re-identification by inferring from neighbors, in: Proceedings of the AAAI Conference on Artificial Intelligence, Vol. 39, 2025, pp. 7356–7364.
- [8] Z. Dai, G. Wang, W. Yuan, S. Zhu, P. Tan, Cluster contrast for unsupervised person re-identification, in: Proceedings of the Asian Conference on Computer Vision, 2022, pp. 1142–1160.
- [9] D. Cheng, X. Huang, N. Wang, L. He, Z. Li, X. Gao, Unsupervised visible-infrared person reid by collaborative learning with neighbor-guided label refinement, in: Proceedings of the 31st ACM International Conference on Multimedia, 2023, pp. 7085–7093.
- [10] L. He, D. Cheng, N. Wang, X. Gao, Exploring homogeneous and heterogeneous consistent label associations for unsupervised visible-infrared person reid, *International Journal of Computer Vision* (2024) 1–20.

- [11] M. Ye, Z. Wu, B. Du, Dual-level matching with outlier filtering for unsupervised visible-infrared person re-identification, *IEEE Transactions on Pattern Analysis and Machine Intelligence* (2025).
- [12] B. Yang, J. Chen, M. Ye, Towards grand unified representation learning for unsupervised visible-infrared person re-identification, in: *Proceedings of the IEEE/CVF International Conference on Computer Vision*, 2023, pp. 11069–11079.
- [13] Z. Pang, C. Wang, L. Zhao, Y. Liu, G. Sharma, Cross-modality hierarchical clustering and refinement for unsupervised visible-infrared person re-identification, *IEEE Transactions on Circuits and Systems for Video Technology* (2023).
- [14] B. Yang, J. Chen, M. Ye, Shallow-deep collaborative learning for unsupervised visible-infrared person re-identification, in: *Proceedings of the IEEE/CVF Conference on Computer Vision and Pattern Recognition*, 2024, pp. 16870–16879.
- [15] J. Pearl, M. Glymour, N. P. Jewell, *Causal inference in statistics: A primer*, John Wiley & Sons, 2016.
- [16] T. Kim, S. Shin, Y. Yu, H. G. Kim, Y. M. Ro, Causal mode multiplexer: A novel framework for unbiased multispectral pedestrian detection, in: *Proceedings of the IEEE/CVF Conference on Computer Vision and Pattern Recognition*, 2024, pp. 26784–26793.
- [17] X. Li, Y. Lu, B. Liu, Y. Liu, G. Yin, Q. Chu, J. Huang, F. Zhu, R. Zhao, N. Yu, Counterfactual intervention feature transfer for visible-infrared person re-identification, in: *European Conference on Computer Vision*, Springer, 2022, pp. 381–398.
- [18] Y.-F. Zhang, Z. Zhang, D. Li, Z. Jia, L. Wang, T. Tan, Learning domain invariant representations for generalizable person re-identification, *IEEE Transactions on Image Processing* 32 (2022) 509–523.
- [19] Z. Yang, M. Lin, X. Zhong, Y. Wu, Z. Wang, Good is bad: Causality inspired cloth-debiasing for cloth-changing person re-identification, in: *Proceedings of*

- the IEEE/CVF Conference on Computer Vision and Pattern Recognition, 2023, pp. 1472–1481.
- [20] X. Li, Y. Lu, B. Liu, Y. Hou, Y. Liu, Q. Chu, W. Ouyang, N. Yu, Clothes-invariant feature learning by causal intervention for clothes-changing person re-identification, arXiv preprint arXiv:2305.06145 (2023).
- [21] X.-C. Li, X. Xia, F. Zhu, T. Liu, X.-Y. Zhang, C.-L. Liu, Dynamics-aware loss for learning with label noise, *Pattern Recognition* 144 (2023) 109835.
- [22] J. Han, P. Luo, X. Wang, Deep self-learning from noisy labels, in: *Proceedings of the IEEE/CVF international conference on computer vision*, 2019, pp. 5138–5147.
- [23] Z. Huang, J. Zhang, H. Shan, Twin contrastive learning with noisy labels, in: *Proceedings of the IEEE/CVF Conference on Computer Vision and Pattern Recognition*, 2023, pp. 11661–11670.
- [24] X. Zhang, Y. Ge, Y. Qiao, H. Li, Refining pseudo labels with clustering consensus over generations for unsupervised object re-identification, in: *Proceedings of the IEEE/CVF conference on computer vision and pattern recognition*, 2021, pp. 3436–3445.
- [25] Q. He, Z. Wang, Z. Zheng, H. Hu, Spatial and temporal dual-attention for unsupervised person re-identification, *IEEE Transactions on Intelligent Transportation Systems* 25 (2) (2023) 1953–1965.
- [26] Y. Cho, W. J. Kim, S. Hong, S.-E. Yoon, Part-based pseudo label refinement for unsupervised person re-identification, in: *Proceedings of the IEEE/CVF Conference on Computer Vision and Pattern Recognition*, 2022, pp. 7308–7318.
- [27] J. Shi, Y. Zhang, X. Yin, Y. Xie, Z. Zhang, J. Fan, Z. Shi, Y. Qu, Dual pseudo-labels interactive self-training for semi-supervised visible-infrared person re-identification, in: *Proceedings of the IEEE/CVF International Conference on Computer Vision*, 2023, pp. 11218–11228.

- [28] J. Shi, X. Yin, Y. Chen, Y. Zhang, Z. Zhang, Y. Xie, Y. Qu, Multi-memory matching for unsupervised visible-infrared person re-identification, in: European Conference on Computer Vision, Springer, 2024, pp. 456–474.
- [29] A. Hermans, L. Beyer, B. Leibe, In defense of the triplet loss for person re-identification, arXiv preprint arXiv:1703.07737 (2017).
- [30] E. Arazo, D. Ortego, P. Albert, N. O’Connor, K. McGuinness, Unsupervised label noise modeling and loss correction, in: International conference on machine learning, PMLR, 2019, pp. 312–321.
- [31] K. Xu, J. Ba, R. Kiros, K. Cho, A. Courville, R. Salakhudinov, R. Zemel, Y. Bengio, Show, attend and tell: Neural image caption generation with visual attention, in: International conference on machine learning, PMLR, 2015, pp. 2048–2057.
- [32] C. Jambigi, R. Rawal, A. Chakraborty, Mmd-reid: A simple but effective solution for visible-thermal person reid, arXiv preprint arXiv:2111.05059 (2021).
- [33] A. Wu, W.-S. Zheng, H.-X. Yu, S. Gong, J. Lai, Rgb-infrared cross-modality person re-identification, in: Proceedings of the IEEE international conference on computer vision, 2017, pp. 5380–5389.
- [34] D. T. Nguyen, H. G. Hong, K. W. Kim, K. R. Park, Person recognition system based on a combination of body images from visible light and thermal cameras, *Sensors* 17 (3) (2017) 605.
- [35] Y. Zhang, H. Wang, Diverse embedding expansion network and low-light cross-modality benchmark for visible-infrared person re-identification, in: Proceedings of the IEEE/CVF conference on computer vision and pattern recognition, 2023, pp. 2153–2162.
- [36] M. Ye, J. Shen, G. Lin, T. Xiang, L. Shao, S. C. Hoi, Deep learning for person re-identification: A survey and outlook, *IEEE transactions on pattern analysis and machine intelligence* 44 (6) (2021) 2872–2893.

- [37] X. Wang, R. Girshick, A. Gupta, K. He, Non-local neural networks, in: Proceedings of the IEEE conference on computer vision and pattern recognition, 2018, pp. 7794–7803.
- [38] F. Radenović, G. Tolias, O. Chum, Fine-tuning cnn image retrieval with no human annotation, *IEEE transactions on pattern analysis and machine intelligence* 41 (7) (2018) 1655–1668.
- [39] C. Chen, M. Ye, M. Qi, J. Wu, J. Jiang, C.-W. Lin, Structure-aware positional transformer for visible-infrared person re-identification, *IEEE Transactions on Image Processing* 31 (2022) 2352–2364.
- [40] Q. Zhang, C. Lai, J. Liu, N. Huang, J. Han, Fmcnet: Feature-level modality compensation for visible-infrared person re-identification, in: Proceedings of the IEEE/CVF Conference on Computer Vision and Pattern Recognition, 2022, pp. 7349–7358.
- [41] H. Yu, X. Cheng, W. Peng, W. Liu, G. Zhao, Modality unifying network for visible-infrared person re-identification, in: Proceedings of the IEEE/CVF International Conference on Computer Vision, 2023, pp. 11185–11195.
- [42] J. Shi, X. Yin, D. Zhang, Z. Zhang, Y. Xie, Y. Qu, Two-stage knowledge distillation for visible-infrared person re-identification, *Pattern Recognition* (2025) 111850.
- [43] J. Wang, Z. Zhang, M. Chen, Y. Zhang, C. Wang, B. Sheng, Y. Qu, Y. Xie, Optimal transport for label-efficient visible-infrared person re-identification, in: European Conference on Computer Vision, Springer, 2022, pp. 93–109.
- [44] X. Zhu, L. Dong, X. Chen, X. Zhang, F. Qi, X.-Y. Jing, Confidence guided semi-supervised cross-modality person re-identification, *Pattern Recognition* 165 (2025) 111669.
- [45] Y. Yang, W. Hu, H. Hu, Progressive cross-modal association learning for unsupervised visible-infrared person re-identification, *IEEE Transactions on Information Forensics and Security* (2025).

- [46] Y. Li, Y. Sun, Y. Qin, D. Peng, X. Peng, P. Hu, Robust duality learning for unsupervised visible-infrared person re-identification, *IEEE Transactions on Information Forensics and Security* 20 (2025) 1937–1948. doi:10.1109/TIFS.2025.3536613.
- [47] D. Cheng, L. He, N. Wang, D. Zhang, X. Gao, Semantic-aligned learning with collaborative refinement for unsupervised vi-reid: D. cheng et al., *International Journal of Computer Vision* (2025) 1–23.
- [48] H. Park, S. Lee, J. Lee, B. Ham, Learning by aligning: Visible-infrared person re-identification using cross-modal correspondences, in: *Proceedings of the IEEE/CVF international conference on computer vision*, 2021, pp. 12046–12055.
- [49] M. Yang, Z. Huang, P. Hu, T. Li, J. Lv, X. Peng, Learning with twin noisy labels for visible-infrared person re-identification, in: *Proceedings of the IEEE/CVF conference on computer vision and pattern recognition*, 2022, pp. 14308–14317.
- [50] Y. Feng, F. Chen, G. Sun, F. Wu, Y. Ji, T. Liu, S. Liu, X.-Y. Jing, J. Luo, Learning multi-granularity representation with transformer for visible-infrared person re-identification, *Pattern Recognition* 164 (2025) 111510.
- [51] Z. Pang, L. Zhao, Y. Liu, G. Sharma, C. Wang, Inter-modality similarity learning for unsupervised multi-modality person re-identification, *IEEE Transactions on Circuits and Systems for Video Technology* 34 (10) (2024) 10411–10423.
- [52] L. van der Maaten, G. Hinton, Visualizing data using t-sne. *journal of machine learning research* 9, Nov (2008) (2008).
- [53] D. Cournapeau, G. members, scikit-learn, <https://scikit-learn.org/stable/index.html> (2007).
- [54] M. Ester, H.-P. Kriegel, J. Sander, X. Xu, et al., A density-based algorithm for discovering clusters in large spatial databases with noise, in: *kdd*, Vol. 96, 1996, pp. 226–231.